# In-situ phase control of a low-loss membrane-based lithium-niobate polarisation-state modulator

MORRIS MWANGI,[1,2,*] Florent Behague,[1,3] Antoine Coste,[1] Jassem Safioui,[4] Miguel Suarez,[1] Jean Byiringiro,[2] Philippe Lutz,[1] Cédric Clévy,[1] and Nadège Courjal[1]

[1]*FEMTO-ST institute, Univ. Bourgogne-Franche-Comté, 25000 Besançon, France*
[2]*Dedan Kimathi University of Technology, 10100 Nyeri, Kenya*
[3]*Kapteos SAS, Bât. Cleanspace 354 voie Magellan, Z.A. Alpespace, 73800 Sainte-Hélène-du-Lac, France*
[4]*Femto-Engineering, 25000 Besançon, France*
*morris.mwangi@femto-st.fr*

**Abstract:** We report on lithium niobate intermediate-thin films with reduced energy-manufacturing costs for manufacturing low-loss electro-optic components. A micrometer-thick membrane surrounded with tapers is inscribed in a single step by smoothly dicing the bottom face of a standard LiNbO$_3$ electro-optic modulator. Hence, we demonstrate a freestanding polarisation-state modulator with insertion losses as low as 2.6 dB. The in-situ structuring of the membrane allows a giant phase control extending over 40°. These developments open the way to a new generation of membrane-based electro-optic devices with low manufacturing-energy costs and reduced yield losses for sensing, telecommunications, or quantum photonics applications.

## 1. Introduction

Since their advent in the 1990s, lithium niobate on insulator (LNOI) wafers have paved the way for dense photonic integrated systems such as dual-comb interferometers [1], or polarisation scramblers [2]. Their acoustic-optical, electro-optical and non-linear properties make them attractive for many applications, from quantum circuits [3] to high-bit-rate telecommunications [4,5]. The sub-micrometer thickness of LNOI-based wafers is crucial for dense integration due to the tight light confinement inside the waveguides, which allows short bending radii [6]. LNOI-based wafers also enhance the electro-optic performances by narrowing the electrodes gap, which decreases the half-wave voltage compared to standard techniques [7]. But LNOI-based wafers are produced through energy-consuming ion-slicing-based processes. The initial 200 keV ion implantation step corresponds to an electric energy consumption of more than 400 kWh, and needs to be combined with four other steps: dielectric deposition, bonding, thermal treatment and polishing [8].

On the other hand, intermediate-thin LiNbO$_3$ films can also provide light confinement, but at reduced manufacturing-energy costs. These intermediate films are micrometer thick and share with LNOI the ability to enhance the electro-optic performances in terms of velocity matching, electro-optic overlap [9], and reduction of substrate-mode coupling losses [10]. The usual manufacturing technique relies on direct bonding followed by lapping-polishing [11], and requires less than 20 kWh to thin and polish the substrate from 500 μm to several micrometers. This technique is well-appreciated in combination with dicing for non-linear applications such as optical parametric amplification [12] or second harmonic generation [13]. But the resulting ridges are multimode, and their vertical profile hinders electrode deposition, thereby limiting electro-optical (EO) applications.

In [14], we reported on an alternative manufacturing method, leading to the serial production of micrometer-thick monomode photonic building blocks with coplanar electrodes. While ion-slicing requires five manufacturing steps, we achieved the membrane and its tapers in a single dicing-polishing step. Moreover, this technique allows insertion losses as low as 2.8 dB, which is comparable to the state-of-the-art in LNOI [15] but without the need for ultra-high numerical aperture fibers. Thereby, we demonstrated an amplitude modulator with a giant EO efficiency of 40 pm/V due to enhanced tip effects, 1.6 times superior to LNOI-based EO devices [16,17].

Here we decline the low-energy-cost production process to the demonstration of a low-loss membrane-based polarisation-state modulator with a giant phase control extending over 40°. The operating point is set by shaping the membrane during the thinning process or by ex-post-facto laser structuring. The proposed techniques address the need for in-situ operating-point adjustment without any waveguide damage.

## 2. Polarisation state modulator

Figure 1 depicts the membrane-based polarisation-state modulator. The component is an X-cut Z-propagating lithium niobate waveguide, and the suspended membrane has the dual purpose of confining the light and providing efficient phase control. A straight channel made by titanium indiffusion ensures light guiding, and the coplanar electrodes surrounding the waveguide transfer the electric signal to the photonic signal as in standard modulators. A single low-energy dicing step suffices to write both the membrane and the tapers simultaneously and produces the free standing membrane [14].
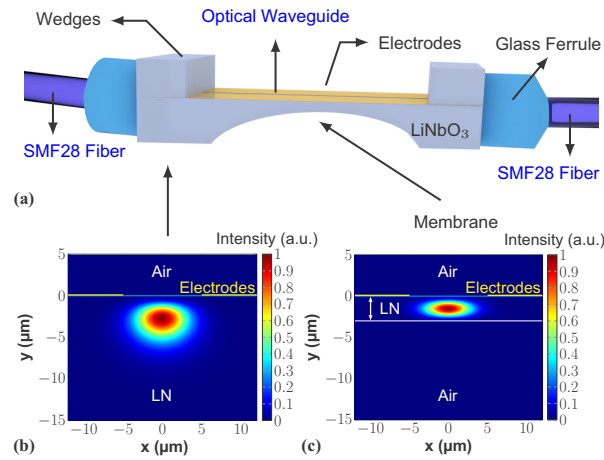


**Fig. 1.** Membrane-based polarisation-state modulator. (a) Scheme of the pigtailed modulator. (b) Optical mode at the waveguide extremities. (c) Optical mode inside the membrane. Calculations performed by finite element method with the COMSOL software.

This polarisation-state modulator changes the output polarisation state by inducing a phase difference $\Delta\varphi$ between the quasi-TE and quasi-TM guided modes as shown in Eq. (1):

$$\Delta\varphi = \varphi_{int} + \frac{\pi \cdot V}{V_\pi} \tag{1}$$

where $V_\pi$ is the half-wave voltage, $V$ the applied voltage and $\varphi_{int}$ is the operating phase, which is related to the waveguide's modal birefringence, $\Delta n_m$, as expressed in Eq. (2):

$$\Delta\varphi_{int} = \int_0^L \frac{2 \cdot \pi \cdot \Delta n_m(z)}{\lambda} dz \tag{2}$$

The active length $L$ coincides with the waveguide's length, and $\lambda$ denotes the wavelength. The control of $\Delta\varphi_{int}$ is crucial for the modulator's performance. Here we show how the membrane contributes to fixing $\Delta\varphi_{int}$ through either thickness control or ex-post-facto laser structuring.

The manufacturing of the modulator begins with a 6-μm-wide titanium rib oriented along the Z-crystal axis and diffused at 1050 °C for 9 hours. A 400-nm-thick silica buffer layer is then evaporated onto the waveguides, and 200-nm-thick Ti-Au electrodes are sputtered afterwards to apply an electric field along the Y-axis. The last optical-grade dicing step patterns the membrane and the tapers. More precisely, the 3350 DISCO DAD dicing saw blade enters the bottom face of the wafer with a rotation speed of 10,000 rpm and a moving speed of 0.2 mm/s, forming a μm-thick membrane with polished surfaces. Noteworthy, the dicing parameters allow a simultaneous surface polishing. The two smooth tapers resulting from the circular blade shape allow an overlap of 85% between the waveguide extremity and the SMF28 fiber. Additionally, the wedges made of LiNbO$_3$ are bonded using UV adhesive on the extremity of the waveguide to facilitate smooth separation of the chips and to increase the pigtailing surface. Finally, the membrane based polarisation state modulator is wire bonded to a printed circuit board and butt-coupled to SMF28 single mode fibers using a NOA170 high-refractive index UV adhesive. Compared to ion slicing techniques, the limited number of steps results in a significant reduction in energy consumption, estimated at 250 kWh for one hundred membranes.

The freestanding 3-μm-thin section of the waveguide reduces by three times the mode's vertical half-width-at-half-maximum compared to the waveguide extremities, as shown in the optical mode spatial distribution intensity of Fig. 1. A BOSA 200 component analyzer is used to measure the characteristic signals of the pigtailed modulator by connecting its input and output to either side of the modulator through SMF28 fibers. The plots in Fig. 2 show the transmission and reflection signals for a 12.6 mm-long membrane-based waveguide. The reflection response is lower than −47 dB over the C-band for both guided polarisations, confirming the taper's ability to convert the optical mode with negligible return losses. The insertion losses of −2.6 dB for the quasi-TE mode and −2.2 dB for the quasi-TM mode clearly illustrate the low coupling losses (0.8 dB/facet) between the standard SMF28 fibers and the waveguide.
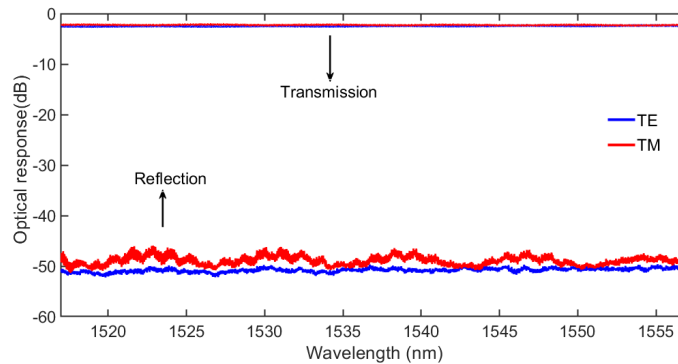


**Fig. 2.** Transmission (top) and reflection (bottom) losses of the membrane-based waveguide. The configuration allows strong light confinement in the membrane without any compromise on the losses.

Since the optical mode geometry also determines its anisotropy, we propose membrane shaping as an effective way to fix the waveguide's birefringence and the associated operating phase. Using Finite Element Method (FEM), we calculated the evolution of the birefringence as a function of the thickness of membranes from 2 μm to 10 μm. We also prepared eight membranes with thicknesses from 1.5 to 7.6 μm. Their output polarisation state was tested with a Keysight N7781B polarimeter. The corresponding operating phase is derived from the Poincaré sphere

following Eq. (3):

$$\Delta \varphi_{int} = \pm (\tan^{-1}(\frac{S_3}{S_2}) + 2 \cdot p \cdot \pi) \qquad (3)$$

where *S3* and *S2* are the Poincaré sphere coordinates, and *p* is the birefringence order. The numerical results reported in Fig. 3(a) show that changing the membrane thickness from 10 to 2 μm allows a birefringence variation from $\Delta n_m = 1.15 \times 10^{-4}$ R.I.U to $4.85 \times 10^{-3}$ R.I.U. The corresponding $\Delta \varphi_{int}$ phase control extends over more than 360°, i.e. more than a period of the sinusoid electro-optic response [Eq. (1)]. The experimental results in Fig. 3(b) confirm a giant phase change of $\delta \Delta \varphi_{int} = 664°$ when thinning the membrane from 500 μm down to 1.5 μm. Noteworthy, if the thickness is larger than 10 μm, the phase change is no longer noticeable and corresponds to the birefringence of a standard waveguide.
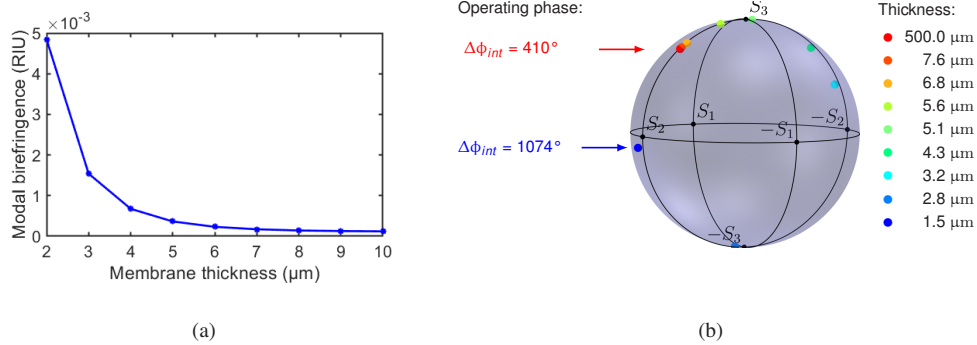


**Fig. 3.** (a) Evolution of the effective birefringence as a function of membrane thickness (F.E.M. calculation). (b) Poincaré sphere showing the evolution of polarisation state as a function of thickness (experimental results for waveguides with a length of *L* = 12.6 mm fabricated in the same conditions but having different membrane thicknesses).

When the membrane thickness is fixed, we propose another approach based on dynamic laser structuring to change a posteriori the operating point. This approach allows an in-situ birefringence control on pigtailed modulators.

## 3. In-situ birefringence control

The approach consists in engraving a hole in the membrane center, but far enough from the waveguide to avoid any optical damage. When a high energy laser pulse is focused on a target surface, the energy generated makes the material sublime and erodes the surface. The high-temperature gradient generates a meta-stable phase in the surrounding material causing changes in its structural and mechanical properties [18]. Here we quantify the effect of these changes by an example of a 10 μm × 100 μm hole engraved 100 μm far from the waveguide by laser ablation. This is achieved with a tangerine Amplitude femtosecond laser at a wavelength of 1030 nm, with a frequency of 5 kHz, a sweep velocity = 0.2 mm/s and number of loops of 10. Each impulsion lasts 230 fs, bringing an energy of 10 μJ. The picture in Fig. 4(a) shows the pigtailed freestanding EO modulator exposed to laser illumination thanks to a 10× objective.

Figure 4(b) depicts the scheme of the experimental setup. The N7781B Keysight high-speed polarimeter is connected to the waveguide output to keep track of the light polarisation evolution during laser illumination. The transmitted optical power is recorded during the structuring, and a function generator connected to the electrodes monitors the waveguide EO properties. As illustrated by the results in Fig. 5, two steps can be distinguished. The first step, laser illumination induces a global birefringence variation as high as $1.02 \times 10^{-4}$ R.I.U. This step is also accompanied by a 0.15 mW decrease of the transmitted power. Then, relaxation occurs
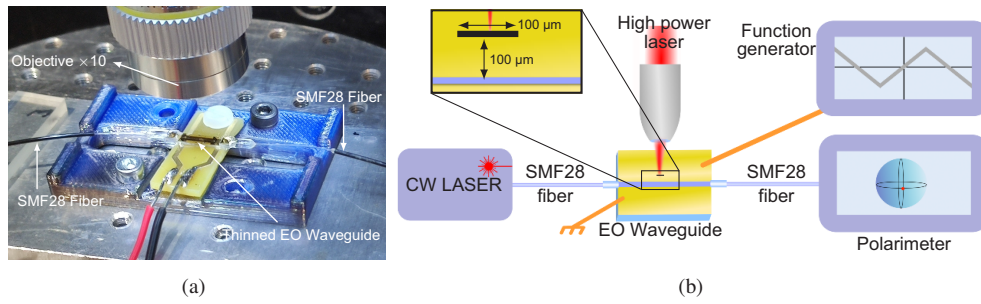
**Fig. 4.** Dynamic structuring of the birefringence. (a) Picture of the pigtailed waveguide before laser structuring. (b) Schematic diagram of the setup for in-situ birefringence structuring.

during 40 s, so that the final transmitted power shows a reduction of only 0.03% compared to the initial situation, which can be considered as negligible. In contrast, the remaining global birefringence change is of $0.15 \times 10^{-4}$ R.I.U., which represents a phase change of $\Delta\varphi_{int} = 44°$, without any impact on the insertion losses. The phase change is confirmed in Fig. 5(d) by the electro-optic modulation figures before and after the laser structuring. Indeed the two modulation paths are similar, but with a shift of $\alpha = 44°$ between each other, deduced from the shift between the blue curve and the red curve on the Poincaré sphere.
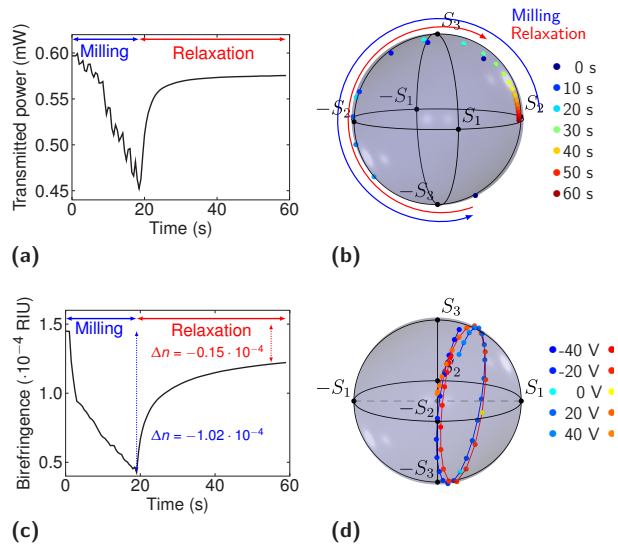


**Fig. 5.** Evolution of the transmitted optical signal state during and after femto-second laser exposition. (a) Evolution of the transmitted power. (b) Evolution of the polarisation state. (c) Birefringence variations deduced from the Poincaré sphere. (d) Figure of modulation before (blue) and after (red) laser structuring.

To reconstruct the electro-optical modulation and evaluate the electro-optic changes induced by laser structuring, we perform the product between the waveguide's Stokes vector $\vec{S_l}$ measured by the polarimeter and the Mueller matrix $M_{pol}$ of a polarizer that would be placed at the exit of the guide with its neutral axis at 45° to the eigenaxes of the guide. Equation (4) gives the stokes

vector $\vec{S}_f$ that would be obtained after the polariser:

$$\vec{S}_f = M_{pol} \cdot \vec{S}_l \tag{4}$$

where,

$$\vec{S}_f = \begin{bmatrix} S_0 \\ S_1 \\ S_2 \\ S_3 \end{bmatrix}, \qquad M_{pol} = \begin{bmatrix} 1 & \cos 2\alpha & \sin 2\alpha & 0 \\ \cos 2\alpha & \cos 2\alpha^2 & \cos 2\alpha \sin 2\alpha & 0 \\ \sin 2\alpha & \cos 2\alpha \sin 2\alpha^2 & \sin 2\alpha^2 & 0 \\ 0 & 0 & 0 & 0 \end{bmatrix},$$

Figure 6 shows the resulting electro-optic modulation, and confirms that the half-wave voltage remains unchanged after the engraving, and equals to 35.2 V. Hence, the hole engraved 100 µm far from the membrane changes only the stress on the waveguide and thereby birefringence, without any damage on the other waveguide's properties.
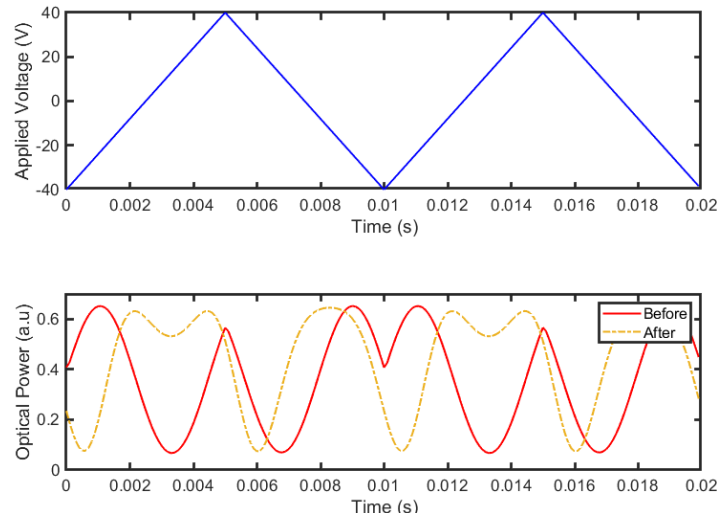


**Fig. 6.** Electro-optical response of the membrane-based modulator. Top: voltage applied on the electrodes. Bottom: in red, the figure of modulation before structuring of the membrane. In orange, the figure of modulation after the structuring of the membrane.

Noteworthy, the measured halfwave voltage is higher than what usually appears in LiNbO$_3$ modulators. Indeed, the waveguide propagates along the Z axis of the crystal to benefit from low intrinsic birefringence. As a result, the halfwave voltage is inversely proportional to $r_{22}$ according to Eq. (5):

$$V_\pi = \frac{\lambda \cdot g}{2 \cdot L \cdot n_o^3 \cdot \Gamma \cdot r_{22}} \tag{5}$$

where $g = 14$ µm is the gap between the electrodes, $L = 12.6$ mm is the active length, $n_o = 2.21$ is the ordinary refractive index at 1.55 µm wavelength, and $\Gamma = 0.67$ is the electro-optic overlap coefficient. Usually, X-cut modulators use a Y-propagation configuration to benefit from the $r_{33}$ coefficient, which is nine times greater than $r_{22}$. Thus, the half-wave voltage can easily be reduced and reach the state-of-the-art by playing on several levers: changing the propagation direction to benefit from the $r_{33}$ coefficient or increasing the active length. Decreasing the g gap is another possibility, as long as $g$ remains higher than the guide width of 6 µm. Work is in progress to model the mechanical behavior of the membrane and deduce the corresponding

birefringence when changing the hole's size and position. Hence, the maximum achievable birefringence will also be quantified.

## 4. Conclusion

In conclusion, we have successfully demonstrated the production of low-loss membrane-based modulators at low energy cost. We have also demonstrated the birefringence monitoring in membrane-based electro-optical modulators, either by thickness control or by structuring the membrane far from the waveguide. These results open the way to new post-processing technologies, which are promising for reducing yield losses during the production of polarisation state modulators.

**Disclosures.** The authors declare no conflicts of interest.

**Data availability.** Data underlying the results presented in this paper are not publicly available at this time but may be obtained from the authors upon reasonable request.

## References

1. A. Shams-Ansari, M. Yu, Z. Chen, C. Reimer, M. Zhang, N. Picqué, and M. Lončar, "Thin-film lithium-niobate electro-optic platform for spectrally tailored dual-comb spectroscopy," Commun. Phys. **5**(1), 88 (2022).
2. Z. Lin, Y. Lin, H. Li, M. Xu, M. He, W. Ke, H. Tan, Y. Han, Z. Li, D. Wang, X. S. Yao, S. Fu, S. Yu, and X. Cai, "High-performance polarization management devices based on thin-film lithium niobate," Light: Sci. Appl. **11**(1), 93 (2022).
3. S. Saravi, T. Pertsch, and F. Setzpfandt, "Lithium niobate on insulator: An emerging platform for integrated quantum photonics," Adv. Opt. Mater. **9**(22), 2100789 (2021).
4. M. Xu, M. He, Y. Zhu, S. Yu, and X. Cai, "Flat optical frequency comb generator based on integrated lithium niobate modulators," J. Lightwave Technol. **40**(2), 339–345 (2022).
5. G. Chen, K. Chen, R. Gan, Z. Ruan, Z. Wang, P. Huang, C. Lu, A. P. T. Lau, D. Dai, C. Guo, and L. Liu, "High performance thin-film lithium niobate modulator on a silicon substrate using periodic capacitively loaded traveling-wave electrode," APL Photonics **7**(2), 026103 (2022).
6. A. Boes, B. Corcoran, L. Chang, J. Bowers, and A. Mitchell, "Status and potential of lithium niobate on insulator (lnoi) for photonic integrated circuits," Laser Photonics Rev. **12**(4), 1700256 (2018).
7. C. Wang, M. Zhang, X. Chen, M. Bertrand, A. Shams-Ansari, S. Chandrasekhar, P. Winzer, and L. Marko, "Integrated lithium niobate electro-optic modulators operating at cmos-compatible voltages," Nature **562**(7725), 101–104 (2018).
8. Y. Jia, L. Wang, and F. Chen, "Ion-cut lithium niobate on insulator technology: Recent advances and perspectives," Appl. Phys. Rev. **8**(1), 011307 (2021).
9. D. Janner, D. Tulli, M. García-Granda, M. Belmonte, and V. Pruneri, "Micro-structured integrated electro-optic linbo3 modulators," Laser Photonics Rev. **3**(3), 301–313 (2009).
10. A. Kanno, T. Sakamoto, A. Chiba, T. Kawanishi, K. Higuma, M. Sudou, and J. Ichikawa, "120-GB/S NRZ-DQPSK signal generation by a thin-lithium-niobate-substrate modulator," IEICE Electron. Express **7**(11), 817–822 (2010).
11. T. Umeki, O. Tadanaga, and M. Asobe, "Highly efficient wavelength converter using direct-bonded ppzlnn ridge waveguide," IEEE J. Quantum Electron. **46**(8), 1206–1213 (2010).
12. T. Kobayashi, S. Shimizu, M. Nakamura, T. Umeki, T. Kazama, R. Kasahara, F. Hamaoka, M. Nagatani, H. Yamazaki, H. Nosaka, and Y. Miyamoto, "Wide-band inline-amplified wdm transmission using ppln-based optical parametric amplifier," J. Lightwave Technol. **39**(3), 787–794 (2021).
13. V. Pecheur, H. Porte, J. Hauden, F. Bassignot, M. Deroh, and M. Chauvet, "Watt-level shg in undoped high step-index ppln ridge waveguides," OSA Continuum **4**(5), 1404–1414 (2021).
14. N. Courjal, A. Caspar, V. Calero, G. Ulliac, M. Suarez, C. Guyot, and M.-P. Bernal, "Simple production of membrane-based LiNbO₃ micro-modulators with integrated tapers," Opt. Lett. **41**(21), 5110–5113 (2016).
15. R. Wu, L. Gao, Y. Liang, Y. Zheng, J. Zhou, H. Qi, D. Yin, M. Wang, Z. Fang, and Y. Cheng, "High-Production-Rate Fabrication of Low-Loss Lithium Niobate Electro-Optic Modulators Using Photolithography Assisted Chemo-Mechanical Etching (PLACE)," Micromachines **13**(3), 378 (2022).
16. B. Pan, H. Cao, Y. Huang, Z. Wang, K. Chen, H. Li, Z. Yu, and D. Dai, "Compact electro-optic modulator on lithium niobate," Photonics Res. **10**(3), 697–702 (2022).
17. A. Prencipe, M. A. Baghban, and K. Gallo, "Tunable Ultranarrowband Grating Filters in Thin-Film Lithium Niobate," ACS Photonics **8**(10), 2923–2930 (2021).

18. U. I. Kalsoom, N. Ali, S. Bashir, A. M. Alshehri, and N. Begum, "Study of micro/nano structuring and mechanical properties of KrF excimer laser irradiated Al for aerospace industry and surface engineering applications," Materials **14**(13), 3671 (2021).